Int J Fract (2006) 141:373–393
DOI 10.1007/s10704-006-9000-2

ORIGINAL PAPER

Multiple cohesive crack growth in brittle materials by the extended Voronoi cell finite element model

Shanhu Li · Somnath Ghosh

Received: 14 October 2005/Accepted: 6 July 2006 / Published online: 20 October 2006

Abstract This paper is aimed at modeling the propagation of multiple cohesive cracks by the extended Voronoi cell finite element model or X-VCFEM. In addition to polynomial terms, the stress functions in X-VCFEM include branch functions in conjunction with level set methods and multi-resolution wavelet functions in the vicinity of crack tips. The wavelet basis functions are adaptively enriched to accurately capture crack-tip stress concentrations. Cracks are modeled by an extrinsic cohesive zone model in this paper. The incremental crack propagation direction and length are adaptively determined by a cohesive fracture energy based criterion. Numerical examples are solved and compared with existing solutions in the literature to validate the effectiveness of X-VCFEM. The effect of cohesive zone parameters on crack propagation is studied. Additionally, the effects of morphological distributions such as length, orientation and dispersion on crack propagation are studied.

Keywords Extended Voronoi cell finite element model · Multi-resolution wavelets · Cohesive zone model · Multiple crack propagation

S. Li · S. Ghosh (✉)
Department of Mechanical Engineering,
The Ohio State University,
650 Ackerman Road, Columbus, OH 43202
USA
e-mail: ghosh.5@osu.edu

1 Introduction

Numerical analysis and simulation of the growth and interaction of multiple cracks in materials is a challenging enterprise due to various kinematic, morphological and constitutive complexities that govern this process. Conventional finite element approaches suffer from very slow convergence since the element formulation does not account for high gradients and singularities. Even a very high density mesh cannot overcome pathological mesh dependence near the crack tips and avoid biasing the direction of crack propagation. The difficulties aggravate significantly in the presence of multiple cracks, due to their interaction with each other. Various methods have been proposed for improving the effectiveness of computational methods in modeling cracks. These include the singular element method using quarter-point elements (Barsoum 1976, 1977; Henshell and Shaw 1975; Hibbit 1977), the method of superposition that introduces singular terms to the finite element interpolations (Yagawa et al., 1980; Yamamoto and Tokuda 1973), or the hybrid singular element methods (Lin and Tong 1980; Piltner 1985; Tong et al. 1973; Tong 1977), which augment interpolation functions using stress intensity factors from classical elasticity theory. While most of these analyses are limited to stationary cracks, it is only in the recent years that effective numerical methods for simulating crack propagation are being proposed.

In this regard, the cohesive zone models or CZM (Camacho and Ortiz 1996; Foulk et al. 2000; Geubelle 1995; Needleman 1987, 1990, 1992; Ortiz and Pandolfi 1999; Tvergaard 1990) have emerged as important tools for modeling crack propagation in homogeneous and heterogeneous materials. A large number of studies e.g. Camacho and Ortiz (1996), Carpinteri (1989) and Xu and Needleman (1994) have simulated crack propagation by inserting special cohesive elements between continuum elements. The use of a highly refined computational mesh, especially near the crack tip is still a requirement, even though the effect is mitigated due to the finite crack tip stress with the CZM. Alternatively, intra-element enrichment approaches, based on the incorporation of embedded discontinuities in displacement or strain fields have been proposed (see Jirasek 2000 for a review), which eliminates mesh dependent prediction of the evolving crack path and hence the need for remeshing. The extended FEM or X-FEM (Belytschko and Black 1999; Belytschko et al. 2001; Dolbow et al. 2000; Moës and Belytschko 2002; Moës et al. 1999) is a powerful recent addition to this family of intra-element enrichment. Cohesive crack propagation has been modeled in this work by using the partition of unity concept to incorporate local enrichment functions that allows the preservation of the general displacement based FEM formalism.

The Voronoi cell finite element method (VCFEM), developed on the principles of the assumed stress hybrid FEM formulation (Tong et al. 1973; Tong 1977), has had considerable success in the micromechanical analysis of multi-phase heterogeneous materials (Ghosh et al. 2000; Ghosh and Moorthy 1998, 2004; Ghosh and Mukhopadhyay 1991; Li and Ghosh 2004, 2006; Moorthy and Ghosh 1996, 2000). By introducing augmentation stress functions having forms that are motivated from analytical micromechanics, the method is able to overcome the need for high resolution mesh in the proximity of morphological discontinuities, such as inclusions, voids, cracks, etc. VCFEM is based on an unstructured mesh of closed polygonal cells as shown in Fig. 1a, where each cell corresponds to the immediate neighborhood of a heterogeneity like an inclusion or crack. While a typical mesh of Voronoi polygons evolves from tessellating a heterogeneous domain (Ghosh and Mukhopadhyay 1991; Ghosh and Moorthy 2004), an element in VCFEM need not adhere to this definition and can be any closed polygonal cell consisting of a heterogeneity in a surrounding matrix. For example, in this paper, each Voronoi element involves a polygonal sub-domain that encompasses an initial crack. Conceptually, VCFEM has a strong resemblance to the mesh-free methods. Each cell in VCFEM represents the neighborhood and region of immediate influence of a heterogeneity, which may be perceived of as the support domain for specially constructed interpolation or kernel functions of field variables and their evolution. A high level of accuracy with significantly reduced degrees of freedom has been achieved with VCFEM in Ghosh et al. (2000); Ghosh and Moorthy (1998, 2004), Ghosh and Mukhopadhyay (1991), Li and Ghosh (2004, 2006) and Moorthy and Ghosh (1996, 2000). Computational efficiency of VCFEM is substantially higher than many conventional FE models. The cohesive crack propagation model has been incorporated in VCFEM in Ghosh et al. (2000) and Li and Ghosh (2004) to model interfacial debonding in fiber reinforced composites. However, in these models, the debonding or crack evolution path is along the interface and hence the cohesive zone regions are known a-priori. In the event that the crack branches off into the matrix, the propagation path is no longer pre-assessed and needs to be determined in each load increment, consistent with the local state of stresses, strains and morphology. This task is considerably more formidable since a slight deviation from the actual path can lead to completely wrong prediction.

Following the trends set in Belytschko et al. (2001), Dolbow et al. (2000), Moës and Belytschko (2002) and Moës et al. (1999), an extended VCFEM or X-VCFEM has been recently developed in (Li and Ghosh 2006) for modeling the growth of multiple cohesive cracks in brittle materials. The model accounts for interaction between cracks and invokes an adaptive crack growth formulation to represent the continuously changing direction of evolving cracks. X-VCFEM augments the conventional VCFEM model by adding multi-resolution wavelet stress functions (Glowinski et al. 1990; Jaffard 1992; Qian and Weiss 1993) in the vicinity of the crack tip, level set based branched functions

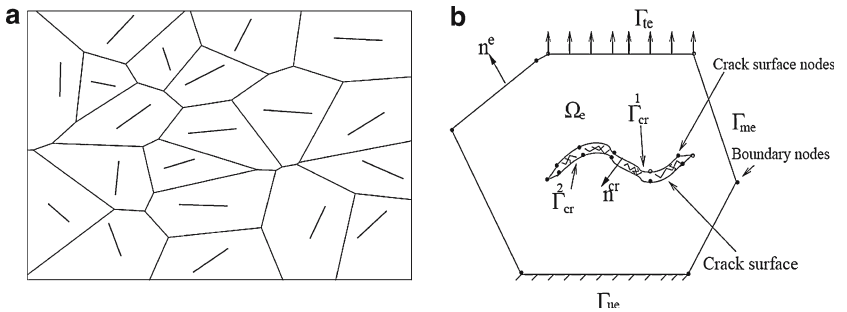

Fig. 1 (**a**) A mesh of Voronoi cell elements, each containing a single pre-existing crack, (**b**) a typical Voronoi cell element showing different topological features and loads

for stress discontinuity across the crack. The incremental crack propagation direction and length are adaptively determined by a cohesive fracture energy based criterion. No remeshing is needed in X-VCFEM for simulating crack growth, and this adds to its desirability and effectiveness. The present paper is an extended the developments in Li and Ghosh (2006) by adding crack merging to its growth mechanism and investigates the predictions of the model for different geometric and constitutive manifestations. It begins with a review of the X-VCFEM formulation and demonstrates its convergence through a numerical example. X-VCFEM is then used to understand the influence of cohesive parameters like peak stress and critical separation, on crack growth in monolithic brittle materials. Subsequently, the effect of morphological distributions including crack interaction, clustering, alignment, etc. on the growth and coalescence are studied as factors critical to the failure process.

2 Summary of X-VCFEM formulation for cohesive cracks

A comprehensive account of the development of the extended Voronoi cell finite element model (X-VCFEM) is given in Li and Ghosh (2006). Figure 1(a) shows a pre-cracked microstructural region Ω with a dispersion of cracks that is tessellated into an unstructured mesh of N polygonal Voronoi cell elements. The topology and constituents of a typical Voronoi cell (VC) element Ω_e are depicted in Fig. 1(b). Although each VC element contains a single crack initially, the adaptive X-VCFEM formulation allows cracks to cross boundaries during the course of their evolution. The fracture process zone for each crack is represented by a cohesive zone model. The element boundary $\partial\Omega_e$ with outward normal $\mathbf{n}^E$ encompasses segments of prescribed traction Γ_{te}, prescribed displacement Γ_{ue} and inter-element boundaries Γ_{me}, i.e. $\partial\Omega_e^E = \Gamma_{te} \bigcup \Gamma_{ue} \bigcup \Gamma_{me}$. The incompatible displacement field across a crack $\Gamma_{\rm cr}$ with a normal $\mathbf{n}^{\rm cr}$ is facilitated through a set of connected node-pairs along the crack length. In the assumed stress hybrid finite element formulation, stationary conditions of the element energy functional in the variational principle yield weak forms of the kinematic equation and traction reciprocity conditions on the boundary and crack face. In an incremental formulation for small deformation elasticity with evolving cracks, the element energy functional Π_e is expressed as:

$$
\begin{aligned}
&\Pi_e(\sigma_{ij}, \Delta\sigma_{ij}, u_i^E, \Delta u_i^E, u_i^{\rm cr}, \Delta u_i^{\rm cr}) \\
&\quad = -\int_{\Omega_e} \Delta B(\sigma_{ij}, \Delta\sigma_{ij}) \mathrm{d}\Omega - \int_{\Omega_e} \epsilon_{ij} \Delta\sigma_{ij} \mathrm{d}\Omega \\
&\qquad + \int_{\partial\Omega_e} (\sigma_{ij} + \Delta\sigma_{ij}) n_j^E (u_i^E + \Delta u_i^E) \mathrm{d}\partial\Omega \\
&\qquad - \int_{\Gamma_{te}} (\bar{t}_i + \Delta\bar{t}_i)(u^E{}_i + \Delta u^E{}_i) \mathrm{d}\Gamma_{te} \\
&\qquad + \int_{\overset{1}{\Gamma}_{\rm cr}} (\sigma_{ij} + \Delta\sigma_{ij}) n_j^{\rm cr} (\overset{1}{u}{}_i^{\rm cr} + \Delta \overset{1}{u}{}_i^{\rm cr}) \mathrm{d}\Gamma_{\rm cr} \\
&\qquad - \int_{\overset{2}{\Gamma}_{\rm cr}} (\sigma_{ij} + \Delta\sigma_{ij}) n_j^{\rm cr} (\overset{2}{u}{}_i^{\rm cr} + \Delta \overset{2}{u}{}_i^{\rm cr}) \mathrm{d}\Gamma_{\rm cr} \\
&\qquad - \int_{\Gamma_{\rm cr}} \int_{\overset{1}{u}{}_i^{\rm cr} - \overset{2}{u}{}_i^{\rm cr}}^{\overset{1}{u}{}_i^{\rm cr} + \Delta \overset{1}{u}{}_i^{\rm cr} - \overset{2}{u}{}_i^{\rm cr} - \Delta \overset{2}{u}{}_i^{\rm cr}} t_i^{\rm coh} \mathrm{d}(\overset{1}{u}{}_i^{\rm cr} - \overset{2}{u}{}_i^{\rm cr}) \mathrm{d}\Gamma_{\rm cr}
\end{aligned}
\tag{1}
$$

where $\boldsymbol{\sigma}$, $\boldsymbol{\varepsilon}$ and $B = (\frac{1}{2}\boldsymbol{\sigma} : \mathbf{S} : \boldsymbol{\sigma})$ are the equilibrated stress field, the corresponding strain fields, and the complimentary energy, respectively in an element interior. $\mathbf{u}^E$ is a kinematically admissible displacement field on the element boundary $\partial\Omega_e^E$ and $\mathbf{u}^{\text{cr}}$ represents displacements on the internal cohesive-crack surfaces Γ_{cr}. Note that body forces are neglected in this formulation. Variables with superscript E are on the element boundary while those with superscripts cr correspond to the crack surface. The prefix Δ denote increments of respective variables. The notations $\overset{1}{(\bullet)}$ and $\overset{2}{(\bullet)}$ represent two sides of the cohesive crack surface in a Voronoi cell element. The last term in Eq. (1) corresponds to work done by cohesive tractions t_i^{coh} due to crack surface separation. The element kinematic equation is satisfied in a weak sense from the stationary condition, obtained by setting the first variation of Π_e in Eq. (1) with respect to stress increments to zero. Weak satisfaction of the traction reciprocity conditions on (i) the inter-element boundary Γ_{me}, (ii) the domain traction boundary Γ_{te} and (iii) the crack surfaces $\overset{1}{\Gamma}_{\text{cr}}$ and $\overset{2}{\Gamma}_{\text{cr}}$ (two sides of the crack) are obtained by setting the first variation of the total energy functional $\Pi = \sum_{e=1}^{N} \Pi_e$ with respect to the displacement fields $\Delta\mathbf{u}^E$, $\Delta\overset{1}{\mathbf{u}}^{\text{cr}}$ and $\Delta\overset{2}{\mathbf{u}}^{\text{cr}}$, respectively to zero.

The cohesive tractions are given by a rate independent extrinsic linear cohesive zone model (Camacho and Ortiz 1996; Ortiz and Pandolfi 1999), which has infinite stiffness at low separations. The effective normal traction-separation response of this model is depicted in Fig. 2 (a, b). The traction across the cohesive surface is expressed in terms of free cohesive fracture energy potential ϕ as:

$$\mathbf{t}^{\text{coh}} = \frac{\partial\phi}{\partial\delta_n}\mathbf{n} + \frac{\partial\phi}{\partial\delta_t}\mathbf{t} = \frac{t}{\delta}(\delta_n\mathbf{n} + \beta^2\delta_t\mathbf{t}) \tag{2}$$

where δ_n and δ_t correspond to the normal and tangential components of the opening displacements over the cohesive surface in the normal ($\mathbf{n}$) and tangential ($\mathbf{t}$) directions, respectively. The magnitude of traction $t = \frac{\partial\phi}{\partial\delta} = \sqrt{t_n^{\text{coh}2} + \beta^{-2}t_t^{\text{coh}2}}$ and the effective opening displacement $\delta = \sqrt{\delta_n^2 + \beta^2\delta_t^2}$. Here t_n^{coh} and t_t^{coh} are the normal and tangential components of surface tractions and β is a coupling coefficient to allow assignment of different weights to normal and tangential opening displacements. For increasing δ, t is expressed as

$$t = \begin{cases} \frac{\sigma_{\max}(\delta_e - \delta)}{\delta_e} & \forall\delta < \delta_e \\ 0 & \forall\delta \geq \delta_e \end{cases} \tag{3}$$

The displacement δ_e is the separation at which t goes to zero and $\sigma_{\max}$ is the peak value of t. Unloading from any point on the traction-separation curve, proceeds along a linear path from the current position to the origin following the relation

$$t = \frac{\sigma_{\max}}{\delta_e}\frac{\delta_e - \delta_{\max}}{\delta_{\max}}\delta \qquad \forall\delta \leq \delta_{\max} \leq \delta_e \tag{4}$$

Reloading occurs with a reduced stiffness in comparison with the original stiffness. For negative normal displacement (compression), stiff penalty springs with high stiffness are introduced between the node-pairs on the crack face.

In X-VCFEM formulation, the equilibrium conditions and constitutive relations in the element interior, as well as the compatibility conditions on the element boundary and crack surface are satisfied a-priori in a strong sense. Equilibrated stress fields in the interior of the element and compatible displacement fields on the element boundaries and crack faces are assumed in this method. In the incremental formulation, equilibriated stress increments are obtained from the stress functions increments $\Delta\Phi(x, y)$, and inter-element compatible displacement fields across the element boundary $\partial\Omega_e^E$ and continuous displacement fields along a crack face $\Gamma_{\text{cr}}^{1/2}$ (superscript 1/2 correspond to two sides of the crack) in an element are generated by interpolation of nodal displacements (Ghosh et al. 2000; Li and Ghosh 2006; Moorthy and Ghosh 1996, 2000). Stress functions are constructed by the superposition of three different components, i.e. $\Phi = \Phi^{\text{poly}} + \Phi^{\text{branch}} + \Phi^{\text{wvlt}}$. The stress increments in an element are computed by adding contributions from each individual function to yield

$$\begin{Bmatrix} \Delta\sigma_{xx} \\ \Delta\sigma_{yy} \\ \Delta\sigma_{xy} \end{Bmatrix}_e = \begin{bmatrix} [\mathbf{P}]^{poly} & [\mathbf{P}]^{branch} & [\mathbf{P}]^{wvlt} \end{bmatrix}_e \begin{Bmatrix} \Delta\beta_{pq} \\ \Delta\beta_{st} \\ \Delta\beta_{m,n,k,l} \end{Bmatrix}_e \tag{5}$$

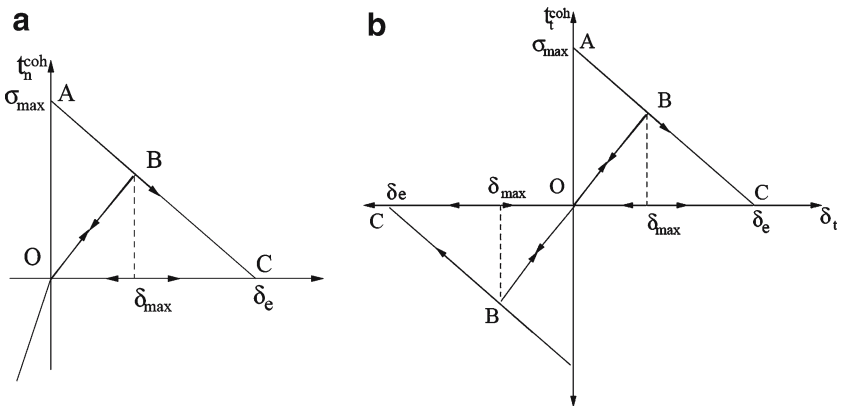

Fig. 2 Normal and tangential traction-separation laws for the extrinsic linear cohesive zone model

$\{\Delta\beta\_e$ is the column of unknown stress coefficient increments associated with the stress interpolation matrix $[\mathbf{P}(x, y)]_e$. The pure polynomial component Φ^{poly} represents far field stresses away from the crack tip. The branch function Φ^{branch} facilitates discontinuity in stresses across the crack surfaces without affecting the solution in the continuous region beyond the crack. For the functional representation of the crack surface, a vector level set method (Belytschko et al. 2001; Sethian 2001; Ventura et al. 2002, 2003) is used. An approximation to the crack surface $\Gamma_{\text{cr}}^{1/2}$ in Fig. 1 is constructed to describe the discontinuous stress fields across crack paths in terms of a signed distance function. The branch stress function increment is constructed in terms of the radial distance and angular functions, based on this function. The multi-resolution wavelet stress function Φ^{wvlt} is constructed from the family of Gaussian functions, i.e.

$$\Delta\Phi_{a,b,c,d}(\xi,\eta) = e^{-(\frac{\xi-b}{a})^2/2} e^{-(\frac{\eta-d}{c})^2/2} \Delta\beta_{a,b,c,d} \quad (6)$$

The dilation and translation parameters (a, c) and (b, d) respectively, can vary in a continuous fashion. By changing the translation parameters, the multi-levels of wavelet bases can be made to closely follow a moving crack tip. The dilation parameter with compact adjustable window support can be used to provide high refinement and resolution near the crack tip. The wavelet based stress function is constructed in a local orthogonal coordinate system (ξ, η) centered at the crack tip, with the ξ direction corresponding to the local tangent at the crack surface. For implementation in multi-resolution analysis involving discrete levels, the translation and dilation parameters should be expressed as discrete multiples of some starting values. Figure 3 shows the distribution of multiple levels of wavelet bases in an extended Voronoi cell element. This region of influence of the wavelet bases is positioned symmetrically about the crack in the vicinity of an evolving crack tips. The crosses $(\times)$ corresponds to the position of each wavelet basis function b_n, d_n at a lower (m) level. As shown in Fig. 3, the squares $(\square)$ correspond to additional locations at a higher level $(m + 1)$ in the multi-resolution algorithm. The region covered by the multi-level wavelet functions reduce successively with levels, but provide higher resolution. Thus the region of influence of the $(m + 1)$-th level wavelets is smaller than that for m-th level. The wavelet enriched incremental stress function in X-VCFEM is thus written as

$$\Delta\Phi^{wvlt}(\xi,\eta) = \sum_{m=1,n=-n_n,k=1,l=-l_n}^{m_n,n_n,k_n,l_n} \Delta\Phi_{m,n,k,l}(\xi,\eta) \quad (7)$$

where the translation parameters n and l range from $-n_n$ and $-l_n$ to n_n and l_n. This allows the wavelets to be positioned symmetrically about the crack (Fig. 3). The addition of higher level wavelet bases to the stress function, marked by squares $(\square)$ in Fig. 3, is done adaptively in accordance with a strain energy based element error measure that has been derived in Li and Ghosh (2006) and Moorthy and Ghosh (2000). The necessary condition for stability, that guarantees non-zero stress parameters $\boldsymbol{\beta}$ for all non-rigid body element boundary/crack

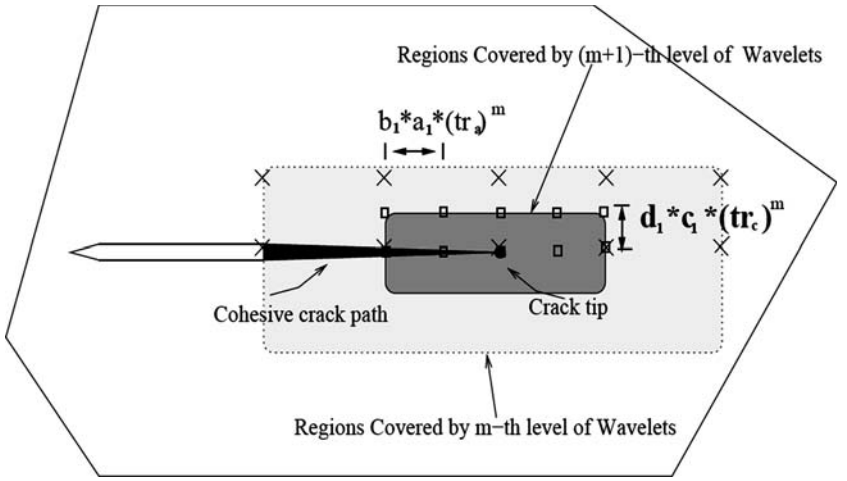

Fig. 3 Schematic diagram of an extended VC element, exhibiting the crack tip region and the surrounding region of multi-level wavelet representation. The crosses (×) corresponds to the position of lower level wavelets and the locations of the adapted higher level wavelet bases are indicated by squares (□)

face displacement fields, is stated as

$$n_\beta > n_q^E + n_q^{\mathrm{cr}} - 3 \tag{8}$$

where n_β is the number of β parameters, and n_q^E and n_q^{cr} are the number of displacement degrees of freedom on the element boundary and crack face respectively.

Solution of the resulting nonlinear equations by a pure Newton–Raphson solver exhibits a discontinuous drop with the evolution of cracks, for cases where the loading process is monotonically controlled by incremental deformation or load conditions. To avert this, the arc-length solver is used through the introduction of an unknown loading parameter to govern the load increments (Crisfield 1981, 1983; Li and Ghosh 2006; Schweizerhof and Wriggers 1986).

3 Cohesive crack propagation and coalescence

Various criteria and conditions govern the evolution of multiple cohesive cracks in an elastic medium. These are discussed next.

3.1 Criterion for direction of incremental crack advance

In X-VCFEM, the incremental crack advance direction is determined from the cohesive fracture energy at the crack tip. From the equivalence of cohesive fracture energy ϕ for complete decohesion and the energy release rate G_c (see Ortiz and Pandolfi 1999), the crack growth direction is estimated as that, along which the cohesive fracture energy ϕ is maximized for a given crack tip state of stress. The cohesive fracture energy ϕ_A at the crack tip A along any direction α can be expressed in terms of the separation $\delta(\alpha)$ in that direction as:

$$\begin{aligned}\phi_A(\alpha) &= \left(\int_0^{\delta(\alpha)} t(\alpha)\mathrm{d}\delta\right)_A \\ &= \left(\int_{\sigma_{\max}}^{t(\alpha)} \sqrt{(t_n^{\mathrm{coh}})^2 + \beta^{-2}(t_t^{\mathrm{coh}})^2}\cdot\frac{\partial\delta}{\partial t}\mathrm{d}t\right)_A\end{aligned} \tag{9}$$

The effective cohesive traction for direction α can be deduced to be

$$t(\alpha) = \sqrt{(\sigma_{xx}\sin^2\alpha - \sigma_{xy}\sin 2\alpha + \sigma_{yy}\cos^2\alpha)^2 + \beta^{-2}(-\frac{1}{2}\sigma_{xx}\sin 2\alpha + \sigma_{xy}\cos 2\alpha + \frac{1}{2}\sigma_{yy}\sin 2\alpha)^2} \tag{10}$$

The incremental direction of crack propagation is assumed as that which maximizes the cohesive fracture energy at A according to the criteria:

$$\frac{\partial \phi_A(\alpha)}{\partial \alpha} = 0 \quad \text{and} \quad \frac{\partial^2 \phi_A(\alpha)}{\partial \alpha^2} < 0 \tag{11}$$

From Eqs. (9) and (10), the criteria (11) is explicitly expressed as

$$\phi_A(\alpha) = \frac{\delta_e}{2\sigma_{\max}}\left(\sigma_{\max}^2 - t(\alpha)^2\right) \tag{a}$$

$$\begin{aligned}
\frac{\partial \phi_A}{\partial \alpha} &= -\frac{\delta_e}{\sigma_{\max}} t \frac{\partial t}{\partial \alpha} = 0 \Longrightarrow \\
\frac{\partial t}{\partial \alpha} &= \frac{1}{\sqrt{\left(\sigma_{xx}\sin^2\alpha - \sigma_{xy}\sin 2\alpha + \sigma_{yy}\cos^2\alpha\right)^2 + \beta^{-2}\left(-\frac{1}{2}\sigma_{xx}\sin 2\alpha + \sigma_{xy}\cos 2\alpha + \frac{1}{2}\sigma_{yy}\sin 2\alpha\right)^2}} \\
&\quad \Bigg[\left(\sigma_{xx}\sin^2\alpha - \sigma_{xy}\sin 2\alpha + \sigma_{yy}\cos^2\alpha\right)\left(\sigma_{xx}\sin 2\alpha - 2\sigma_{xy}\cos 2\alpha - \sigma_{yy}\sin 2\alpha\right) \\
&\quad + \beta^{-2}\left(-\frac{1}{2}\sigma_{xx}\sin 2\alpha + \sigma_{xy}\cos 2\alpha + \frac{1}{2}\sigma_{xx}\sin 2\alpha\right)\left(-\sigma_{xx}\cos 2\alpha - 2\sigma_{xy}\sin 2\alpha + \sigma_{yy}\cos 2\alpha\right)\Bigg] \\
&= 0
\end{aligned} \tag{b}$$

$$\begin{aligned}
\frac{\partial^2 \phi_A}{\partial \alpha^2} &= \frac{\delta_e}{\sigma_{\max}}\Bigg[\left(\sigma_{xy}\sin 2\alpha - \sigma_{xx}\sin^2\alpha - \sigma_{yy}\cos^2\alpha\right) \\
&\quad \times \left(\sigma_{xx}\sin 2\alpha - 2\sigma_{xy}\cos 2\alpha - \sigma_{yy}\sin 2\alpha\right) \\
&\quad + \beta^{-2}\left(\frac{1}{2}\sigma_{xx}\sin 2\alpha - \sigma_{xy}\cos 2\alpha - \frac{1}{2}\sigma_{yy}\sin 2\alpha\right)^2\left(-\sigma_{xx}\cos 2\alpha - 2\sigma_{xy}\sin 2\alpha + \sigma_{yy}\cos 2\alpha\right)\Bigg] \\
&< 0
\end{aligned} \tag{c}$$

(12)

The direction of crack propagation α_c is obtained as the solution of Eq. (12)b as

$$\alpha_c^{XVCFEM} = \begin{cases} \arctan\left(\frac{-\sigma_{xx}+\sigma_{yy} \pm \sqrt{(\sigma_{xx}-\sigma_{yy})^2 + 4\sigma_{xy}^2}}{2\sigma_{xy}}\right) \\ \arctan\left(\frac{2(\beta^2-1)\sigma_{xy} \pm \sqrt{(4\beta^4 - 8\beta^2 + 4)\sigma_{xy}^2 - (4\beta^4 - 4\beta^2 + 2)\sigma_{xx}\sigma_{yy} - (2\beta^2-1)(\sigma_{xx}^2 + \sigma_{yy}^2)}}{2\beta^2\sigma_{xx} - \sigma_{xx} + \sigma_{yy}}\right) \end{cases} \tag{13}$$

The optimal angle α_c^{XVCFEM} is chosen as the one that satisfies the condition in Eq. (12)c.

3.2 Length of the incremental cohesive crack advance

The length of cohesive zone advance ($\Delta\bar{l}$) in the crack evolution scheme is estimated using a criterion that the cohesive fracture energy goes to zero at the end of the new segment as shown in Fig. 4(a). Hence the directional gradient of the cohesive fracture energy plays a role in this criterion. The cohesive fracture energy at two points A (present crack tip) and B (close to A in the direction of crack propagation) are evaluated by substituting the value of the stresses in Eq. (12a). The tip of the cohesive zone is obtained from the linear extrapolation of this line that corresponds to zero cohesive fracture energy. From Fig. 4(a), the increment of cohesive zone for probable crack growth is given by the dimension:

$$\Delta\bar{l} = \frac{\phi_A}{\phi_A - \phi_B}|AB| \tag{14}$$

where $|AB|$ is the distance between the two points in the incremental crack direction.

3.3 Cracks crossing interelement boundaries

Crack advance from one Voronoi cell element to the next occurs in X-VCFEM following an algorithm depicted in Fig. 4(b). A continuous tracking

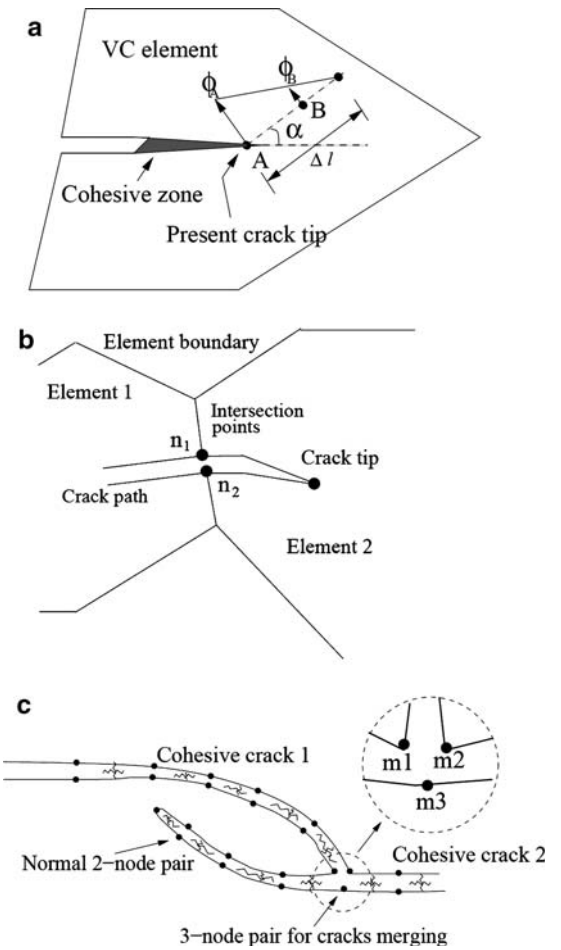

Fig. 4 Algorithms for incremental propagation of cohesive cracks: (**a**) for determining direction and incremental length of the cohesive zone, (**b**) for crossing element boundaries and (**c**) for merging with other cracks

method is implemented to monitor if a cohesive crack surface has reached an element boundary or gone past it. The intersection of the crack surface with an element boundary is first checked by solving the equation system

$$\frac{x - x_i}{x_{i+1} - x_i} = \frac{y - y_i}{y_{i+1} - y_i}, \quad \frac{x - x_n}{x_{n+1} - x_n} = \frac{y - y_n}{y_{n+1} - y_n} \tag{15}$$

where (x_i, y_i) represents the tip of the cohesive crack line for the ith increment, and (x_n, y_n) is the position of the nth node on the element boundary. If the intersection point is outside of the cohesive line or the element boundary, it is assumed that there is no intersection. Once a cohesive crack has reached its intersection with the boundary, a new node pair (n_1, n_2) is introduced on the element boundary at this point as shown in Fig. 4(b). The node pair belongs to the intersection of the element boundary and the cohesive crack, i.e. $n_1 n_2 \in \partial\Omega_e^E \cap \Gamma_{\text{cr}}$. The crack is subsequently advanced to the next element following the intra-element crack advance procedure discussed above.

3.4 Crack coalescence

The coalescence or merging of multiple cracks is also considered is this paper. Figure 4(c) shows the merger of two cohesive cracks. The algorithm for crack merging, outlined below, is an extension of the element boundary intersection algorithm in Sect. 3.3.

- Record all the cracks that have propagated in an increment.

- Check for the intersection of the last incremental segment of the cohesive crack with those of all neighboring cracks that belong to either the same element or neighboring elements, using Eq. (15).
- Insert a three-node junction (m_1, m_2, m_3) at the point of intersection, once intersection of two crack segments is ascertained. This junction is shown in Fig. 4(c).
- Apply cohesive zone models to all node pairs of the three nodes at this junction.
- Contribution of the junctions nodes, e.g. (m_1, m_2), to the load vector in the assembled matrix equation requires special treatment. For each of these nodes, contributions of integrals from adjoining crack segments belonging to two different cohesive cracks are summed.
- As soon as crack tip merges with other cracks, the stress concentration at the crack tip disappears. Consequently, remove the wavelet functions corresponding to this crack tip from the stress functions for the element.

4 X-VCFEM validation for accuracy and efficiency

A set of numerical examples are conducted for validating the accuracy and efficiency of X-VCFEM, prior to its application for parametric studies on multiple crack propagation in brittle media. In this section, three sets of numerical examples are solved and compared with other codes or established results in the literature, for examining the accuracy and efficiency of X-VCFEM. These convergence studies for static and quasi-static cracks augment studies that have been conducted in Li and Ghosh (2006).

4.1 Comparison of a single crack propagation model with ABAQUS

As a benchmark, a static problem of a plate with a single cohesive edge crack is solved using the commercial FEM code ABAQUS and compared with results by X-VCFEM. The problem, schematically depicted in Fig. 5(a), is solved for plane strain conditions under a remote tension load. The material modeled has a Young's modulus $E = 70 \times 10^3$ MPa and Poisson ratio $\nu = 0.33$. A special user element (UEL) subroutine is developed in ABAQUS for incorporating the cohesive model at the crack face. It is difficult to incorporate the extrinsic cohesive model in the displacement based ABAQUS, since there is a stress jump at zero displacement. To circumvent this problem in ABAQUS, a bilinear cohesive zone model discussed in Li and Ghosh (2004) is used to describe crack growth in the plate. The cohesive parameters for this model are $\sigma_{\max} = 5$ MPa, $\delta_c = 1 \times 10^{-6}$ mm, $\delta_e = 5 \times 10^{-3}$ mm and $\beta = 0.707$. The uniform load in the y direction is increased from $0 - 3$ MPa. A total of 12840 QUAD4 elements with 13250 nodes and 77 cohesive elements are used in ABAQUS. In X-VCFEM, the entire domain is represented by a single element consisting of 142 nodes on the boundary and crack faces. Adaptive multi-level enrichment of the wavelet bases is performed by the strain energy criterion (Li and Ghosh 2006). The optimal parameters for stress function representations in X-VCFEM have been determined in Li and Ghosh (2006) to be $p_n = q_n = 13$, $s_n = t_n = 0$, $n_n = 4$, $l_n = 1$, $m_n = k_n = 4$, $a_1 = c_1 = b_1 = d_1 = 0.1$ and $tr_a = tr_c = 0.5$. This corresponds to 102 terms in the polynomial stress function Φ^{poly}, 1 term in the branch function Φ^{branch} and 128 terms in the wavelet function Φ^{wvlt} for a total of 231 terms. This structure of element stress functions is retained for all subsequent simulations. The crack is assumed to propagate horizontally due to problem symmetry and hence, the modules for determining incremental crack direction in Sect. 3 are switched off in this problem. The automatic load stepping algorithm in AQAQUS requires a total of 37 load steps while the X-VCFEM simulation is conducted in 8 steps to reach the desired maximum load. Figure 5(b) shows the load-vertical displacement $(\sigma - u_y)$ plot at the point **A** of the crack face. The load-displacement results by X-VCFEM are in excellent agreement with the high resolution ABAQUS model, thus exhibiting its accuracy. On the other hand, the X-VCFEM simulation takes only 1.6 minutes on a single CPU in the Pentium 4 cluster with 2.4Ghz Intel P4 Xeon processors, as opposed to 13.9 minutes for ABAQUS on the same machine. Even for this simple example, an excess of tenfold advantage in computing speed is achieved by X-VCFEM. This

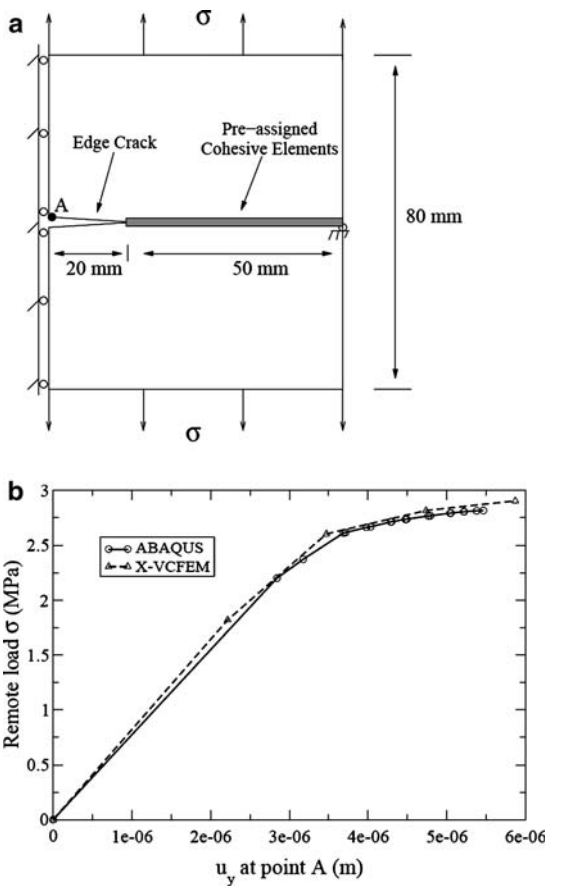

Fig. 5 (**a**) A plate with an edge crack under remote tension load, (**b**) comparison of load-deformation response by X-VCFEM and ABAQUS

factor is expected to increase considerably with increasing complexity, such as more cracks.

Figure 6 shows the contour plot of the load direction stress σ_{yy} and the corresponding stress distributions due to various terms in the stress function at the end of the first load step. The figure in the inset of Fig. 6(c) is a rescaled plot of the stress due to the branch function, since this is orders of magnitude smaller (mode I crack in this problem) than those due to polynomial or wavelet representations. The set of contour plots point to several important observations summarized below.

- The stress distribution due to polynomial terms in Fig. 6(b) describes the stress field far from the crack tip well, but it fails to predict a high gradient around the crack tip.
- The stress distribution due to the branch function in Fig. 6(c) clearly shows its capability to depict stress discontinuity along the crack surface. However, the magnitude of this stress is of the order of 10^{-11}, which is almost trivial compared with contributions from the polynomial and wavelet functions. This is because the stress discontinuity does not exist at the crack face for this mode I problem, as shown in the stress contour plot of Fig. 6(a).
- Figures 6(d, e and f) show stress distributions due to three levels of wavelet functions, respectively. High gradients in the stress component are missed by the low level wavelet functions, but these are represented much better by higher levels of wavelets in the adapted smaller regions. This demonstrates the advantage of the multi-resolution wavelet function representation.

4.2 Comparison with the results of a classical dynamic crack propagation problem

This is a numerical experiments, based on the well known Kalthoff's experiment on dynamic crack

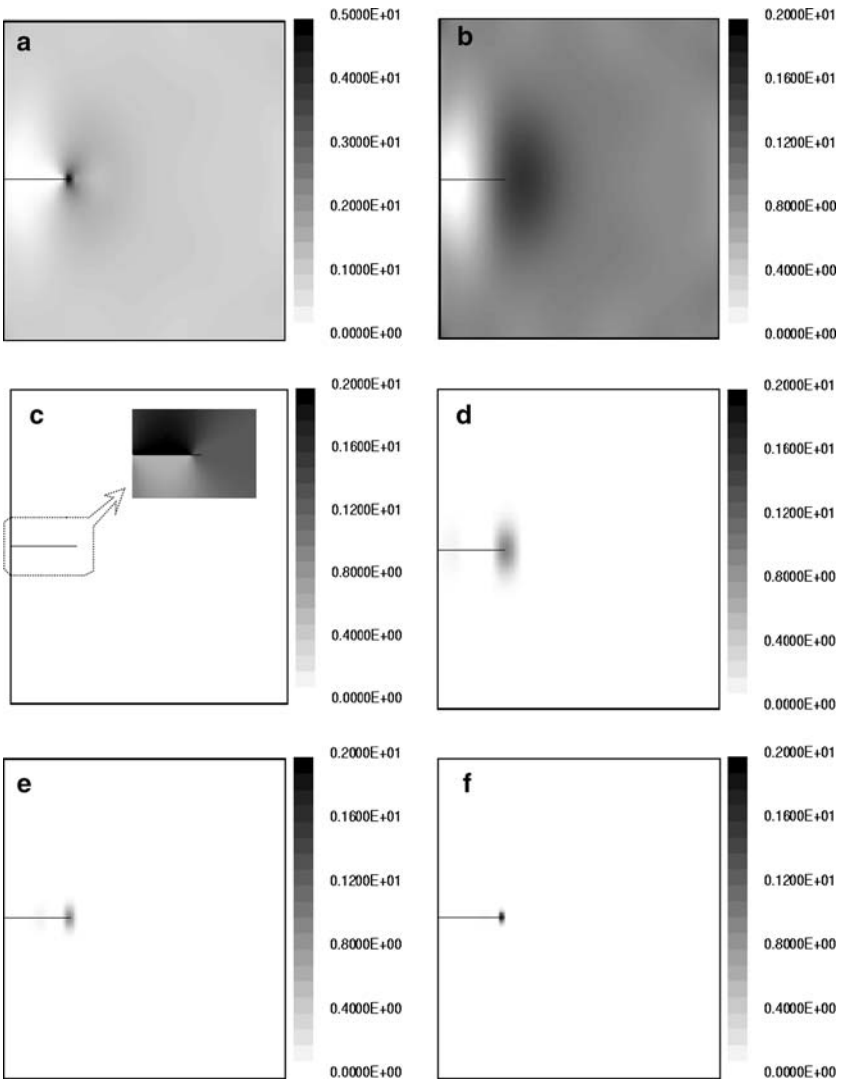

Fig. 6 Contour plot of the load direction stress σ_{yy} and the corresponding distributions due to different terms in the stress functions: (**a**) total σ_{yy}, (**b**) contribution from Φ^{poly}, (**c**) contribution from Φ^{branch} (inset shows a re-scaled contour near the crack face), (**d**) contribution from level-1 Φ^{wvlt}, (**e**) contribution from level-2 Φ^{wvlt}, and (**f**) contribution from level-3 Φ^{wvlt}

propagation in an impact loaded prenotched plate. This problem has been the subject of many studies (Kalthoff 2000; Kalthoff and Winkler 1988; Rethore et al. 2005). The studies suggest that a crack, subjected to a tension-compression load as shown in Fig. 7(a), propagates at an angle of approximately 60–70$^{\text{o}}$ with respect to the initial notch in the plate. The present X-VCFEM development does not incorporate inertia terms, and hence a quasi-static crack propagation problem is simulated instead of the dynamic test. The configuration in Fig. 7(a), shows that the experimental projectile motion is replaced by the traction boundary conditions in the simulation under plane strain conditions. A small initial crack length ($a = 0.02, \frac{a}{b} = 0.11$ in Fig. 7(a)) is chosen to mitigate the effect of the constrained right hand boundary on crack propagation. Material properties for this problem are: Young's modulus $E = 207\,\text{GPa}$ and Poisson ratio $\nu = 0.3$. Since the cohesive zone model parameters corresponding to the experiments are essentially unknown to the authors, the X-VCFEM

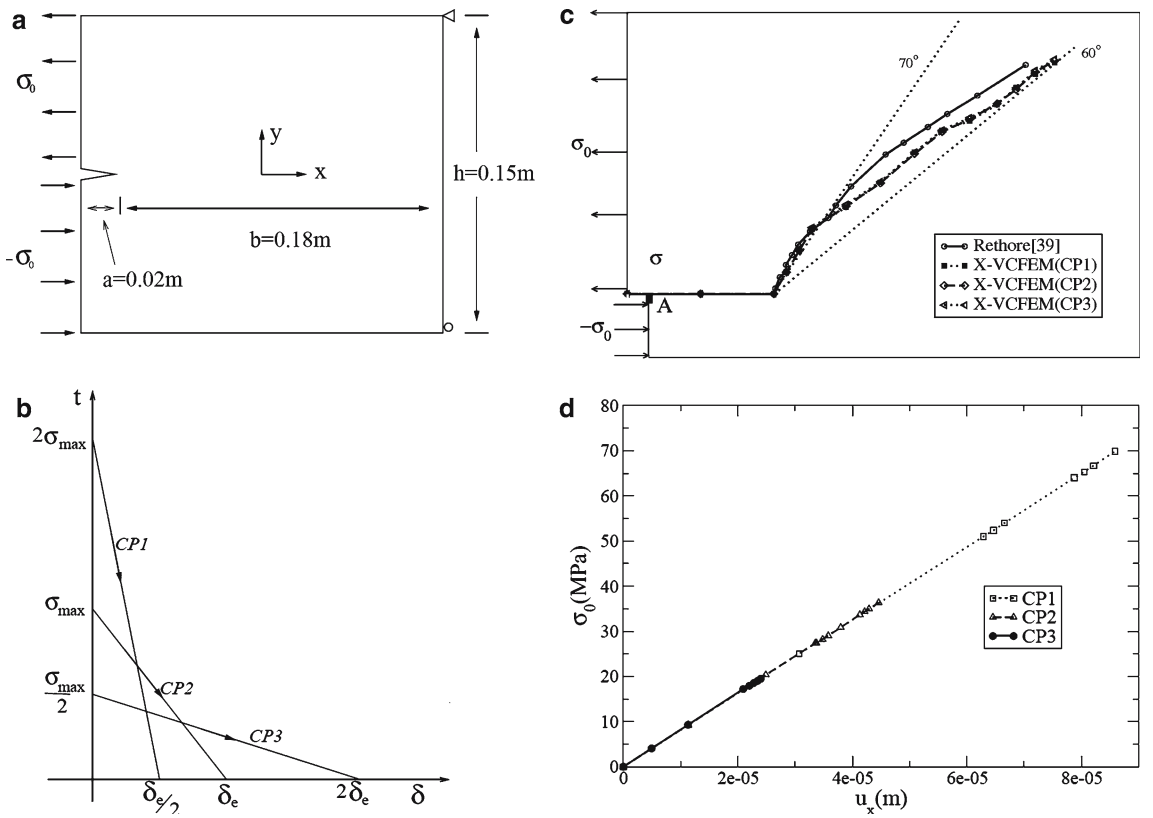

Fig. 7 (**a**) A plate with an edge crack for the classical Kalthoff experiment, (**b**) cohesive models with three different sets of parameters, (**c**) prediction of the crack path by X-VCFEM, and (**d**)applied stress-horizontal displacement plots at point A for different cohesive zone models

simulation is conducted with three sets of cohesive parameters as shown in Fig. 7(b). They are: (i) **CP-1**: $\sigma_{\max} = 40.0\,\text{MPa}$, $\delta_e = 0.6$ e-4m, $\beta = 1$, (ii) **CP-2**: $\sigma_{\max} = 20.0\,\text{MPa}$, $\delta_e = 1.2$ e-4m, $\beta = 1$, and (iii) **CP-3**: $\sigma_{\max} = 10.0\,\text{MPa}$, δ_e=2.4 e-4m, $\beta = 1$. The sets correspond to identical cohesive fracture energy (area under the curve) but different peak stress and critical separation values. The X-VCFEM simulations also investigate the sensitivity of the solutions to the cohesive parameters. The entire computational domain is represented by a single element in X-VCFEM with 132 nodal degrees of freedom. The crack paths, predicted by X-VCFEM simulation for the three sets of cohesive parameters are shown in Fig. 7(c). The initial crack growth angle for all cases is around 70^o. This angle is corroborated by brittle failure experiments at very low velocities in Erdogan and Sih (1963). Subsequently, the crack propagation takes place within the envelope between 60^o and 70^o. This is in agreement with studies in Kalthoff (2000), Kalthoff and Winkler (1988), Rethore et al. (2005). Figure 7(c) also shows that the crack growth path for this problem is not sensitive to the cohesive zone parameters. The dynamic conditions, as well as boundary constraints are responsible for the small difference between X-VCFEM results and those in Rethore et al. (2005). Figure 7(d) shows the plot of the applied stress as a function of the horizontal displacement at the base of the notch at A. A linear response is seen for all the models.

4.3 Crack propagation in a three-point bending specimen

In this example, a mixed-mode cohesive crack propagation is modeled in a three-point bend test with an unsymmetrically positioned initial crack. The

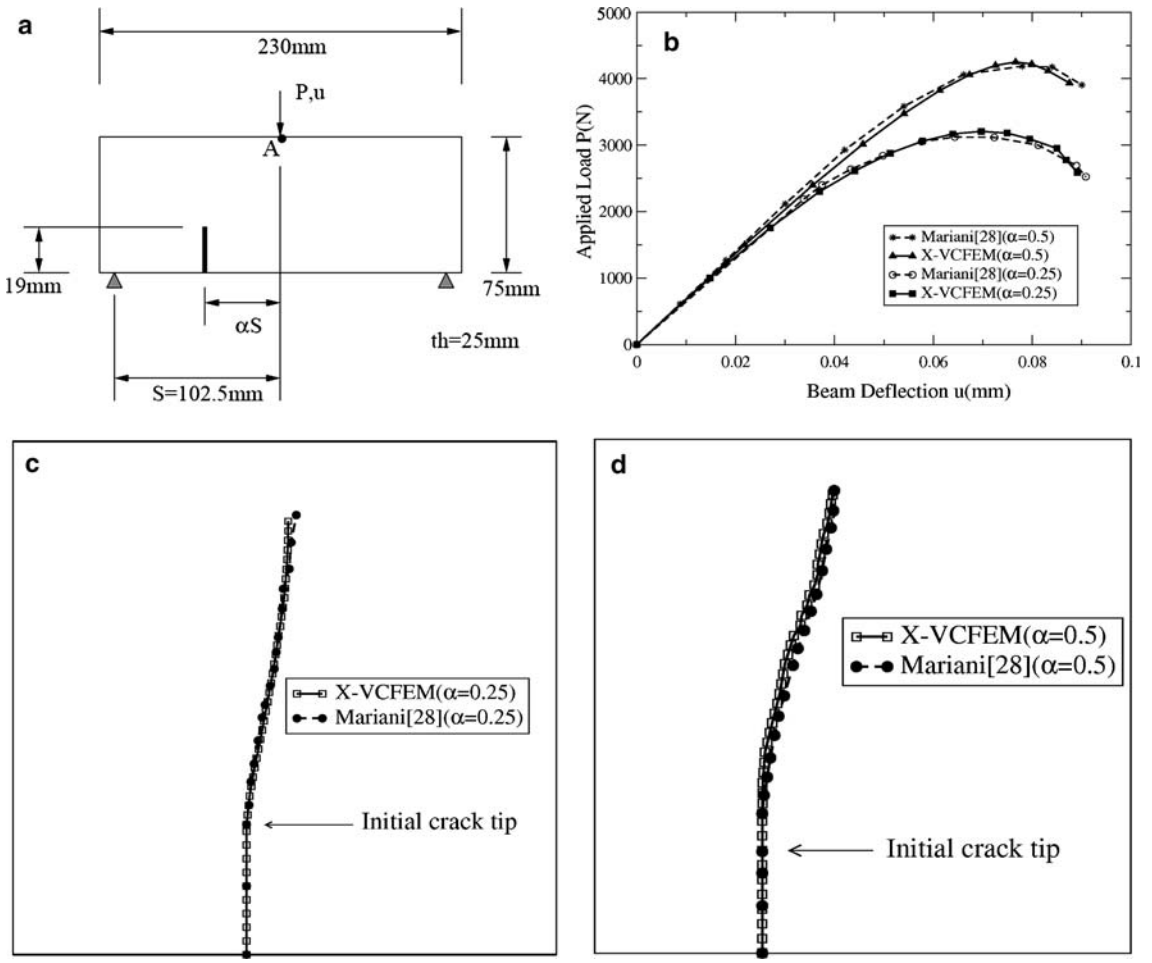

Fig. 8 (**a**) A three-point bending specimen with an unsymmetric initial crack, (**b**) comparison of load-deflection response from results of X-VCFEM (Mariani and Perego 2003) and, (**c**,**d**) comparison of the crack paths by X-VCFEM with that in Mariani and Perego (2003) for $\alpha = 0.25$ and $\alpha = 0.5$ respectively

problem has been studied by Mariani and Perego (2003) using XFEM under plane stress conditions. Figure 8(a) shows the geometrical dimensions, load P at point **A** and boundary constrains. The initial crack position is determined by the offset ratio α, defined as the ratio of the distance of the initial crack from the mid-span cross-section to half of the beam span. The material has a Young's modulus $E = 31,370\,\text{MPa}$ and Poisson ratio $\nu = 0.2$. The cohesive parameters for this problem are **CP1**: $\sigma_{\max} = 4.4$ MPa, $\delta_e = 0.07719298\,\text{mm}$, $\beta = 1$, which have been used in Mariani and Perego (2003). Once again, the entire domain is represented by a single Voronoi element in X-VCEFM with 154 nodal degrees of freedom, and the stress interpolation functions consist of 102 terms in the polynomial stress function, 1 term in the branch function and 128 terms in the wavelet function for a total of 231 terms. The arc-length method explained before is used to govern the load increments so as to describe the softening in load-deflection responses. Figure 8(b) shows the load-deflection curve (at the load point **A**) for two values of the offset parameter, i.e. $\alpha = 0.5$ and $\alpha = 0.25$. The initial elastic response in the load **P**-deflection **u** curve is stiffer and also the peak load is higher for higher values of α. The load-deflection response exhibits significant softening in the later stages of crack propagation due to the extent of the evolved crack. The path of crack propagation for the two cases are shown in Fig. 8(c) and (d). The cracks move towards the point of applied load

and align themselves perpendicular to the edge of the specimen. Excellent agreement is obtained between the results by X-VCFEM and in Mariani and Perego (2003).

5 Effect of cohesive parameters on crack evolution

Cohesive zone model parameters, e.g. $\sigma_{\max}$ and δ_e in Eq. 3, can significantly affect crack propagation and the overall behavior of a cracking material. Issues related to the implementation of cohesive zone models for the process zone in a crack path have been discussed in detail in Elices et al. (2002) and Yang and Cox (2005). In Elices et al. (2002), it has been argued that intrinsic models with a hardening branch followed by a softening branch extend a cohesive crack to a zone with large number of cracks, thus inhibiting localized cracking. Furthermore, the intrinsic models use a high initial hardening slope, which results in mesh dependence of the solution and very small elements are necessary near the fracture surface. An extrinsic model, which consists of a monotonically decreasing traction function, is consequently a desirable model especially in the absence of an explicitly defined crack path. However, for displacement-based finite element analysis, the extrinsic models face a major problem arising from the stress jump at $\delta = 0$. This requires regularization for stability, and consequently the intrinsic models are preferred with displacement based FEM. Stress intensity factors (K_I and K_{II}) and the J-integral are used as alternatives to traction at the crack tip. In comparison, the assumed stress based X-VCFEM can provide the stress explicitly at the crack tip without depending on the displacements, and hence is an advantageous method with the extrinsic cohesive models. This section considers the effect of various parameters in the extrinsic cohesive model, as well as the morphology e.g. distribution and orientation of pre-existing cracks, on their evolution.

5.1 Crack propagation in a three-point bending specimen

This example revisits the three-point bend simulation in Sect. 4.3 with three different sets of cohesive parameters, to examine their effect on crack propagation. The cohesive parameters are:

- **CP1**: $\sigma_{\max} = 4.4\,\text{MPa}$, $\delta_e = 0.07719298\,\text{mm}$, (highest peak stress, lowest critical displacement)
- **CP2**: $\sigma_{\max} = 2.2\,\text{MPa}$, $\delta_e = 0.15438596\,\text{mm}$
- **CP3**: $\sigma_{\max} = 1.1\,\text{MPa}$, $\delta_e = 0.30877192\,\text{mm}$ (lowest peak stress, highest critical displacement)

The coefficient $\beta = 1$ in Eq. 2 for all cases. The simulations are carried out till softening behavior is observed in the load-displacement response. Figure 9(a) is a plot of the applied load to the deflection of the point of application of the load. Significant sensitivity to the cohesive parameters is seen in these plots. The load-deflection response exhibits softening in the later stages of crack propagation due to the significantly evolved crack. The stiffness of the **P-u** curve is higher for higher values of the peak stress $\sigma_{\max}$. On the other hand, larger δ_e's in **CP2** and **CP3** delay relatively the onset of softening for the cases with smaller peak stresses during the damage process. The path of crack propagation for the three cases are shown in the Fig. 9(b). The cracks move towards the point of applied load and align themselves perpendicular to the edge of the specimen. The crack growth path does not depend significantly on the cohesive parameters.

5.2 Crack growth in a sheared plate

Crack propagation in a plate with a central crack was experimentally studied by Erdogan and Sih (1963), where the plate was subjected to a far field shear load. An optical micrograph of the cracked specimen in Erdogan and Sih (1963) is shown in Fig. 10(a). The material of the specimen in the experiment was assumed to be homogeneous, isotropic and linearly elastic and the crack was assumed to be brittle. This problem is simulated by X-VCFEM with a single element of dimension $10 \times 8\,\text{cm}$ as shown in Fig. 10(c). The initial crack length is $\mathbf{l_0} = 1.6\,\text{cm}$. The material parameters are: Young's modulus $E = 100\,\text{GPa}$, Poisson ratio $\nu = 0.3$. Since the cohesive parameters have not been assessed in the experiments, the

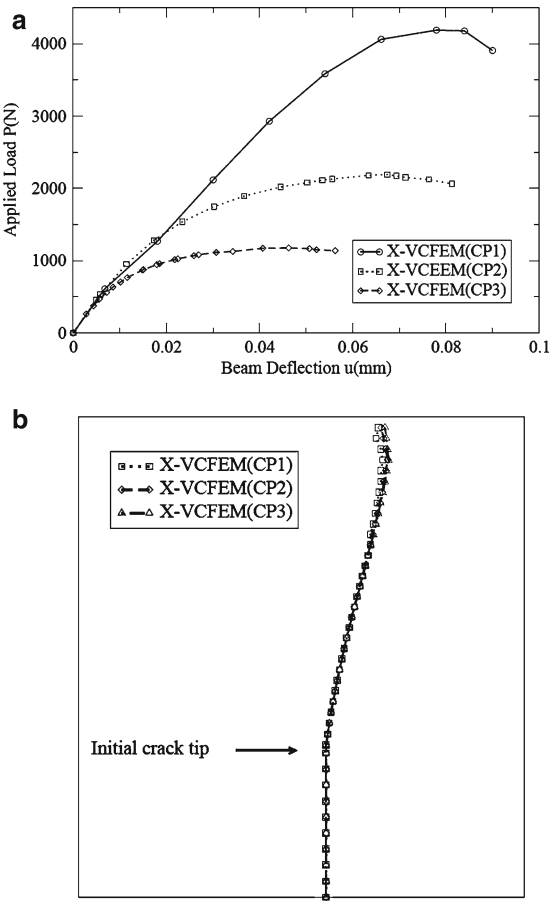

Fig. 9 (**a**) Comparison of load-deflection behavior and (**b**) the crack paths by X-VCFEM for different cohesive zone parameters with $\alpha = 0.5$

sensitivity of the solution to five different sets of cohesive parameters is studied in the simulations. These sets, illustrated in Fig. 10(b) correspond to the same cohesive fracture energy and are:

- **CP1:** $\sigma_{\max}$=3.0 MPa, $\delta_e = 3.0 \times 10^{-3}$ mm
- **CP2:** $\sigma_{\max}$=6.0 MPa, $\delta_e = 1.5 \times 10^{-3}$ mm
- **CP3:** $\sigma_{\max}$=3.0 MPa, $\delta_e = 6.0 \times 10^{-3}$ mm
- **CP4:** $\sigma_{\max}$=6.0 MPa, $\delta_e = 3.0 \times 10^{-3}$ mm
- **CP5:** $\sigma_{\max}$=1.5 MPa, $\delta_e = 6.0 \times 10^{-3}$ mm

The coefficient $\beta = 1$ in Eq. 2 for all cases. In Fig. 10(c), a uniform shear load per unit length τ_0 is applied on the top and bottom surfaces. The load increment is applied by controlling the incremental crack propagation (Li and Ghosh 2006). A total of 8 load increments are applied to execute this problem. In each increment, the applied load is scaled by the arc-length parameter (Li and Ghosh 2006) to yield an equilibrated applied load corresponding to a prescribed crack propagation length.

The crack paths predicted by X-VCFEM for all the different cohesive parameters compare very well with experimental observations in Erdogan and Sih (1963). The path shows very little sensitivity to the cohesive parameters. However the cohesive parameters have a significant influence on the shear load response as a function of the crack length. This is demonstrated in Fig. 10(d), where the normalized crack length is defined as $l_r = \frac{\text{current crack length}}{\text{initial crack length}}$. Thus the crack propagation rate, but not its direction is dependent on the cohesive parameters. For the cases with larger peak traction i.e. **CP2** and **CP4**, higher applied loads are needed for causing similar extent of crack growth as for **CP1** and **CP3** with lower peak stresses. Comparison of the results for parameters **CP2** and **CP4** show that a smaller δ_e results in quicker reduction of the local cohesive traction. This makes the overall load with **CP2** to increase slower than that with **CP4** corresponding to a higher δ_e. The result with

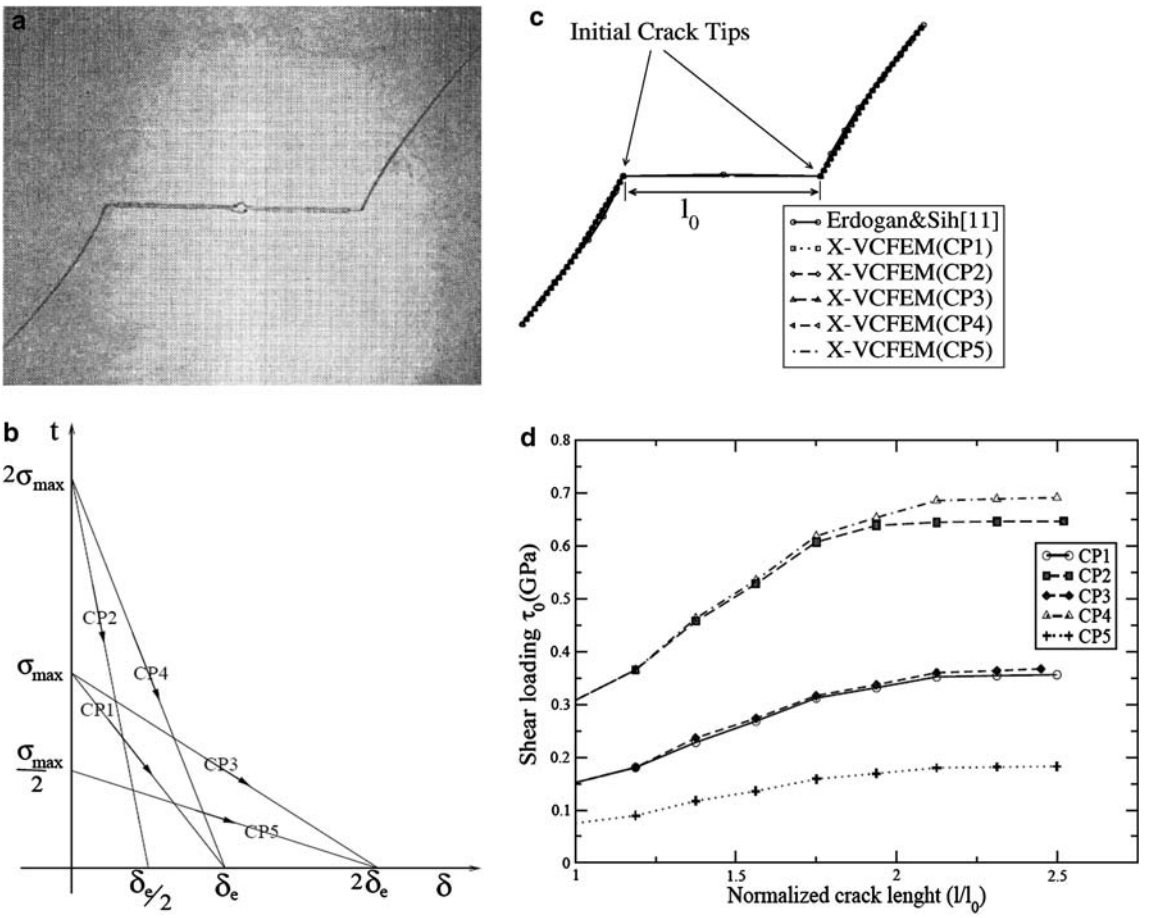

Fig. 10 (**a**) Optical micrograph showing the path of cracking in a plate with a central crack subjected to far-field shear (Erdogan and Sih 1963), (**b**) 5 different sets of cohesive parameters for X-VCFEM simulations, (**c**) corresponding crack paths generated by X-VCFEM, (**d**) comparison of the growth of cracks for the different parameters

parameters **CP5** is consistent with the trends exhibited with the other parameters. Although the simulation results show that both $\sigma_{\max}$ and δ_e affect the crack growth, comparison of cases **CP1**, **CP2**, **CP3** with **CP4** shows that the crack growth is more sensitive to $\sigma_{\max}$ than to δ_e. The results also imply that the cohesive fracture energy or effectively the energy release rate G_c does not alone determine the crack propagation behavior. Individual parameters, affecting the shape of the cohesive law, play an important role in predicting growth characteristics.

5.3 Propagation of multiple cracks in a plate

A plate with 28 randomly located and oriented cracks is simulated under a tensile loading in this example. Figure 11(a) and (b) show the two microstructures with different crack distributions. For the *microstructure 1*, cracks of equal length are randomly dispersed but are oriented horizontally. The *microstructure 2* has cracks of random length and orientation. In addition, it contains a cluster of 8 cracks in an otherwise random distribution as shown in Fig. 11(b). The plate is of dimension 0.1×0.1 m, and the material parameters are: Young's modulus $E = 10^4$ MPa and Poisson ratio $\nu = 0.3$. The Voronoi cell mesh in Fig. 11(a) consists of 694 nodal degrees of freedom on the cell boundaries and 1004 nodal degrees of freedom on the cracks. On the other hand, the mesh in Fig. 11(b) consists of 650 nodal degrees of freedom on the cell boundaries and 1008 nodal degrees of freedom on the cracks. The stress interpolation

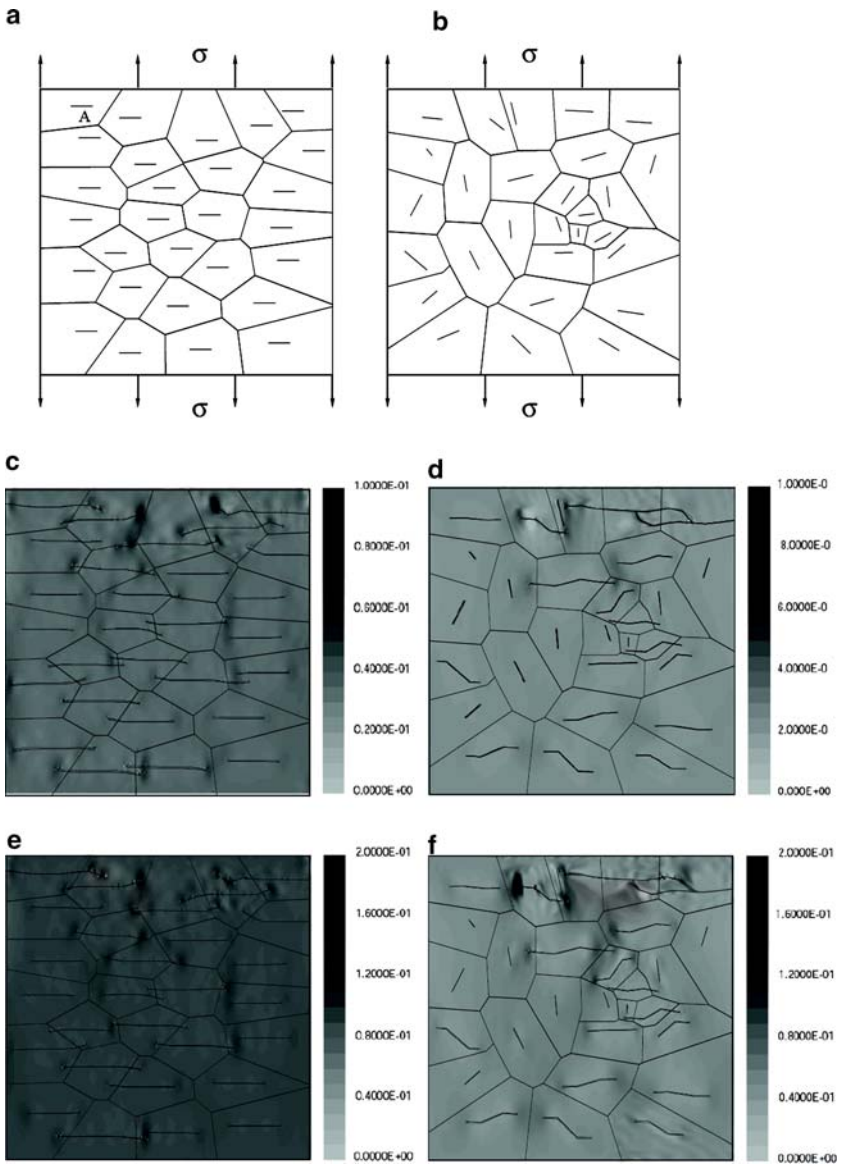

Fig. 11 Crack propagation in two square micro-regions containing 28 cracks, by X-VCFEM: (**a**) domain with horizontal cracks of equal length and random distribution, (**b**) domain with random orientation, length and distribution of cracks but containing a cluster, (**c**,**d**) contour plots of σ_{yy} (MPa) with cohesive parameters *CP1* for the domains in (**a**) and (**b**), (**e**,**f**) contour plots of σ_{yy} (MPa) with cohesive parameters *CP2* for the domains in (**a**) and (**b**)

functions for each element are the same as discussed before. As a crack crosses the element boundary or merges with another crack, the wavelet terms in the stress interpolations are adjusted following the procedure described in Sect. 3.4. To understand the effect of the cohesive parameters on crack propagation, two different sets of cohesive parameters are considered:

- **CP1**: $\sigma_{\max}$=1.0 MPa, δ_e=1.0 e-5 m, $\beta = 0.707$
- **CP2**: $\sigma_{\max}$=2.0 MPa, δ_e=0.5 e-5 mm, $\beta = 0.707$

A uniform tension load σ per unit length is applied on the top and bottom surfaces as shown in Fig. 11(a,b). The applied load is increased in a total of

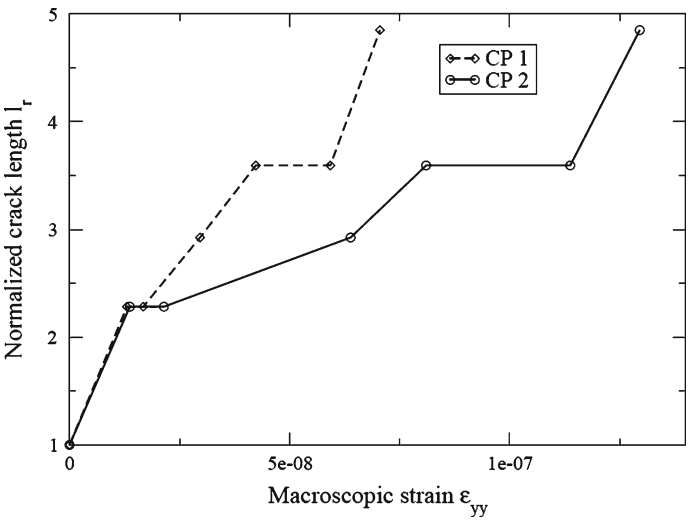

Fig. 12 Comparison of the growth of crack **A** in *microstructure 1* with different cohesive parameters

9 increments and is scaled by the arc-length parameter for load equilibrium corresponding to a prescribed crack opening.

Figure 11(c,d) and (e,f) show the stress σ_{yy} contour plots along with evolved position of the cracks for the two sets of microstructures and cohesive parameter, respectively. The plots are shown for the final load increment. The growth pattern of each crack can be observed by comparing with its initial configuration in Fig. 11(a) and (b). The cracks propagate across element boundaries, interact with each other and in some cases merge. The dependence of the propagation of multiple cracks on the morphology and cohesive parameters is complicated, in general. However, several observations can be made based on the results of the X-VCFEM simulations.

- Larger stress concentrations develop at tips of cracks that are nearly perpendicular to the direction of loading. Consequently, this subset of cracks grows more easily than others that are more aligned with the loading direction. From Fig. 11(d) and (f), it can be seen that some cracks that are nearly parallel to the load direction never propagate.
- Stress concentrations are higher at tips of the longer cracks. For the same external load, sections corresponding to longer cracks leave less intact material, leading to higher stress concentrations. As a consequence, it is seen in Fig. 11(d) and (f) that the longer cracks propagate more than the shorter ones.
- Irrespective of the initial orientation, the evolved crack path tends to align in a direction perpendicular to the applied load direction. This corresponds to an optimal direction for releasing the cohesive fracture energy. This observation is dominant, when the influence of nearby cracks on the local stress field is small. The local stress field in this case is mainly governed by the influence of the applied load on this single crack.
- Cracks are attracted towards weak surfaces, such as other cracks or voids and prefer to propagate in those directions. This may be attributed to the fact that the cohesive fracture energy in the direction of these weaker surfaces with lower (or zero) tractions is naturally lower in comparison with other directions. Higher crack tip hoop stress appears on the side close to the weak surface, e.g. near another crack. This drives the crack propagation in that direction towards the other crack, eventually resulting in a merger. Once a crack merger occurs, the high concentrated stresses no longer exist near the merged regions, and hence the crack ceases to propagate further.
- Cracks in the two configurations of Fig. 11(a) and (b) behave very differently due to the evolution of local stress and cohesive energy. Even though the two cracks at the upper right corner are initially not that dissimilar, their final

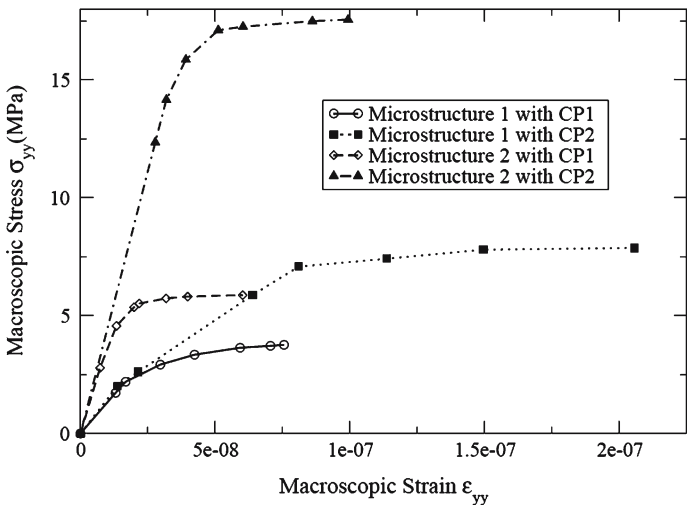

Fig. 13 Macroscopic stress–strain response for different microstructural morphologies and cohesive parameters

configurations in the Fig. 11(e) and (f) are quite different. Different crack mergers are observed for these two cases. For Fig. 11(a), the crack on the upper right hand corner propagates to the domain boundary and this causes a big change in the stress state at the crack tip, affecting the crack propagation direction. While the two cracks at the upper right corner of Fig. 11(a) do not merge, they do in Fig. 11(b) due to different evolving stress states.

- Figure 11(d) and (f) show that the longest crack does not necessarily evolve from a cluster. Not all cracks in a cluster grow considerably. This is somewhat in contrast to observations made with particle reinforced composites, where almost always clusters cause a local stress concentration. The interaction between neighboring cracks contributes to the enhancement or mitigation of stresses, depending on their orientations and length. This dictates their propagation and just being in a cluster does not guarantee significant growth.
- Different cohesive parameters show very little difference in the final configuration and hence the propagation direction. However, the rate of crack growth varies considerably with these parameters as seen in the crack length-macroscopic strain plot of Fig. 12.

Figure 13 shows the macroscopic stress–strain response for the two microstructures and cohesive parameters. Even before the cracks propagate (signaled by the change in slope), the stiffness of the *microstructure 2* is higher than that of *microstructure 1* due to a higher level of effective damage caused by crack lengths and more importantly orientations. Orientations perpendicular to the load direction cause a larger reduction in stiffness in comparison with other directions. With additional loading, the overall damage caused by the growth of cracks is also higher for the *microstructure 1*. This is seen by the lower values of the macroscopic stress for this case. The effect of the cohesive parameters on the stress–strain response is quite pronounced. The maximum macroscopic stress for both microstructures increases significantly for higher values of $\sigma_{\max}$, even though the cohesive fracture energy is the same for the two cohesive models. This is caused by a slowdown in the growth rate of the cracks with overall deformation.

6 Concluding remarks

In this paper, an extended Voronoi cell finite element model or X-VCFEM developed in Li and Ghosh (2006) is further augmented to accommodate crack coalescence. The resulting X-VCFEM model is used to predict multiple crack interaction and propagation in brittle materials. X-VCFEM incorporates special enhancements to the stress functions in a hybrid assume stress element formulation to the element to allow stress discontinuities across the cohesive crack and to accurately depict the crack tip stress concentrations. These features are accommodated through the incorpo-

ration of branch functions in conjunction with level set methods across crack contours, and adaptive multi-resolution wavelet functions in the vicinity of the crack tip. This results in a powerful numerical model that avoids the use of cumbersome remeshing or mesh refinement with growing cracks. The cracks are modeled by an extrinsic cohesive zone model, for which the stress jump at zero displacement can be easily modeled by the hybrid stress-based VCFEM. This is a special advantage of VCFEM, which can use extrinsic models and thus avoid intrinsic models that show mesh dependence. A particular focus of this paper is on the effect of cohesive parameters on crack growth. The incremental growth directions and lengths of these cracks are adaptively determined in terms of cohesive fracture energy near the crack tip.

Various problems are solved with X-VCFEM and compared with existing solutions in the literature to validate the model and show convergence. The X-VCFEM results show excellent accuracy and efficiency in comparison with other numerical solutions and experimental solutions in the literature. Numerical simulations with X-VCFEM are then used to understand the effect of different cohesive parameters on the crack propagation. In addition to the total cohesive fracture energy, individual cohesive parameters have significant effect especially on the rate of crack growth. However, the path of growth for single cracks is relatively unaffected by the change in cohesive parameters. Finally, a problem with multiple cracks is analyzed to study the effect of morphology, e.g. length, position and orientations of cracks on their propagation and interaction. The simulations reveal that longer cracks that are nearly perpendicular to loading direction are more amenable to grow larger at a faster rate than other cracks. The crack propagation direction is also dependent on the local stress field, which is a function of both the external load and local morphology, such as other cracks in the neighborhood. In the recent years X-FEM has proven to be an effective tool modeling moving discontinuities without the need for continuous remeshing. X-VCFEM is also a significant addition to this family. It has been proven to be a powerful tool for analyzing large regions of the microstructure with multiple growing and interacting cracks. Research is now underway for extending the evolving crack problem to heterogeneous microstructures with inclusions.

Acknowledgements This work has been partially supported by the Air Force Office of Scientific Research through grant No.F49620-98-1-01-93 (Program Director: Dr. B. L. Lee) and by the Army Research Office through grant No. DAAD19-02-1-0428 (Program Director: Dr. B. Lamattina). This sponsorship is gratefully acknowledged. Computer support by the Ohio Supercomputer Center through grant PAS813-2 is also gratefully acknowledged.

References

Barsoum RS (1976) On the use of isoparametric finite elements in linear fracture mechanics. Int J Numer Meth Eng 10:25–37

Barsoum RS (1977) Triangular quarter-point elements as elastic and perfectly-plastic crack tip elements. Int J Numer Meth Eng 11:85–98

Belytschko T, Black T (1999) Elastic crack growth in finite elements with minimal remeshing. Int J Numer Meth Eng 45:601–620

Belytschko T, Moes N, Usui A, Parimi C (2001) Arbitrary discontunities in finite element. Int J Numer Meth Eng 50:993–1013

Camacho GT, Ortiz M (1996) Computational modeling of impact damage in brittle materials. Int J Solid Struct 33:2899–2938

Carpinteri A (1989) Finite deformation effects in homogeneous and interfacial fracture. Eng Fract Mech 32:265–278

Crisfield MA (1981) A fast incremental/iterative solution procedure that handles 'snap-through'. Comput Struct 13:55–62

Crisfield MA (1983) An arc-length method including line searches and accelerations. Int J Numer Meth Eng 19:1269–1289

Dolbow J, Moes N, Belytschko T (2000) Discontinuous enrichent in finite elements with a partition of unity method. Finite Elem Anal Des 36(3–4):235–260

Elices M, Guinea GV, Gomez J, Planas J (2002) The cohesive zone model: advantages, limitations and challenges. Eng Fract Mechan 69:137–163

Erdogan F, Sih GC (1963) On the crack extension in plates under plane loading and transverse shear. J Basic Eng 519–527

Foulk JW, Allen DH, Helms KLE (2000) Formulation of a three-dimensional cohesive zone model for application to a finite element algorithm. Comput Meth Appl Mechan Eng 183:51–66

Ghosh S, Ling Y, Majumdar B, Ran K (2000) Interfacial debonding analysis in multiple fiber reinforced composites. Mechan Mater 32:561–591

Ghosh S, Moorthy S (1998) Particle cracking simulation in non-uniform microstructures of metal-matrix composites. Acta Metallurigica et Materialia 46:965–982

Ghosh S, Mukhopadhyay SN (1991) A two dimensional automatic mesh generator for finite element analysis of

randomly dispersed composites. Comput Struct 41:241–256
Ghosh S, Moorthy S (2004) Three dimensional Voronoi cell finite element model for modeling microstructures with ellipsoidal heterogeneities. Comput Mechan 34:510–531
Glowinski R, Lawton W, Ravachol M, Tenenbaum E (1990) Wavelet solutions of linear and nonlinear elliptic, parabolic and hyperbolic problems in one space dimension. Comput Meth Appl Sci Eng. SIAM, Philadelphia, PA
Geubelle PH (1995) Finite deformation effects in homogeneous and interfacial fracture. Int J Solid Struct 32:1003–1016
Henshell RD, Shaw KG (1975) Crack tip finite elements are unnecessary. Int J Numer Meth Eng 9:495–507
Hibbit HD (1977) Some properties of singular isoparametric element. Int J Numer Meth Eng 11:180–184
Jaffard S (1992) Wavelet methods for fast resolution of elliptic problem. SIAM J Numer Anal 29:965–986
Jirasek M (2000) A comparative study on finite elements with embedded discontinuities. Comput Meth Appl Mechan Eng 188:307–330
Kalthoff JK (2000) Modes of dynamic shear failure in solids. Int J Fract 101:1–31
Kalthoff JK, Winkler S (1988) Failure mode transition at high rates of loading. Proceedings of the international conference on impact loading and dynamics behaviour of materials. Chiem CY, Kunze HD, Meyer LW (eds) 43–56
Li S, Ghosh S (2004) Debonding in composite microstructures with morphologic variations. Int J comput meth 1:121–149
Li S, Ghosh S (2006) Extended Voronoi cell finite element model for multiple cohesive crack propagation in brittle materials. Int J Numer Meth Eng 65:1028–1067
Lin KY, Tong P (1980) Singular finite elements for the fracture analysis of v-notched plate. Int J Numer Meth Eng 15:1343–1354
Mariani S, Perego U (2003) Extended finite element method for quasi-brittle fracture. Int J Numer Meth Eng 58:103–126
Moës N, Belytschko T (2002) Extended finite element method for cohesive crack growth. Int J Numer Meth Eng 69:813–833
Moës N, Dolbow J, Belytschko T (1999) A finite element method for crack growth without remeshing. Eng Fract Mechan 46(1):131–150
Moorthy S, Ghosh S (1996) A model for analysis for arbitrary composite and porous microstructures with Voronoi cell finite elements. Int J Num Meth Eng 39: 2363–2398
Moorthy S, Ghosh S (2000) Adaptivity and convergence in the Voronoi cell finite element model for analyzing heterogeneous materials. Comput Meth Appl Mechan Eng 185:37–74
Needleman A (1987) A continuum model for void nucleation by interfacial debonding. J Appl Mechan 54:525–531
Needleman A (1990) An analysis of decohesion along an imperfect interface. Int J Fract 42:21–40
Needleman A (1992) Micromechanical modeling of interfacial decohesion. Ultramicroscopy 40:203–214
Ortiz M, Pandolfi A (1999) Finite-deformation irreversible cohesive element for three-dimensional crack-propagation analysis. Int J Numer Meth Eng 44:1267–1282
Qian S, Weiss J (1993) Wavelets and the numerical solution of boundary value problems. Appl Math Lett 6:47–52
Piltner R (1985) Special finite elements with holes and internal cracks. Int J Numer Meth Eng 21:1471–1485
Rethore J, Gravouil A, Combescure A (2005) An energy-conserving scheme for dynamic crack growth using the eXtended finite element method. Int J Numer Meth Eng 63:631–659
Schweizerhof KH, Wriggers Y (1986) Consistent linearization for path following methods in nonlinear F.E. analysis. Comput Meth Appl Mechan Eng 59:261–279
Sethian JA (2001) Evolution, implementation, and application of level set and fast marching methods for advancing fronts. J Comput Phys 169:503–555
Tvergaard V (1990) Effect of fiber debonding in a whisker-reinforced metal. Mater Sci Eng A 125:203–213
Ventura G, Xu JX, Belytschko T (2002) A vector level set method and new discontinuity approximations for crack growth by EFG. Int J Numer Meth Eng 54:923–944
Ventura G, Budyn E, Belytschko T (2003) Vector level sets for description of propagating cracks in finite elements. Int J Numer Meth Eng 58:1571–1592
Tong P, Pian THH, Lasry SJ (1973) A hybrid-element approach to crack problems in plane elasticity. Int J Numer Meth Eng 7:297–308
Tong P (1977) A hybrid crack element for rectilinear anisotropic material. Int J Numer Meth Eng 11:377–403
Xu XP, Needleman A (1994) Finite deformation effects in homogeneous and interfacial fracture. J Mechan Phys Solid 42:1397–1434
Yagawa Y, Aizawa T, Ando Y (1980) Crack analysis of power hardening materials using a penalty function and superposition method. Proc 12th Conf Fract Mechan, ASTM STP 700:439–452
Yamamoto Y, Tokuda N (1973) Determination of stress intensity factor in cracked plates by the finite element method. Int J Numer Meth Eng 6:427–439
Yang Q, Cox B (2005) Cohesive models for damage evolution in laminated composites. Int J Fract 133:107–137